Check for updates

Research Article | Vol. 30, No. 14 / 4 Jul 2022 / Optics Express 25219

Optics EXPRESS

# Optical net gain measurement on $Al_{0.07}Ga_{0.93}N$/GaN multi-quantum wells

QUANG MINH THAI,[1] SERGI CUESTA,[2] LOU DENAIX,[2] SYLVAIN HERMELIN,[1] OLIVIER BOISRON,[1] EDITH BELLET-AMALRIC,[2] CATHERINE BOUGEROL,[3] FLORIAN CASTIONI,[4] STEPHEN T. PURCELL,[1] LE SI DANG,[3] AND EVA MONROY[2,*]

[1] *Institut Lumière Matière, CNRS, University of Lyon, Univ. Claude Bernard Lyon 1, 69622 Villeurbanne, France*
[2] *Univ. Grenoble-Alpes, CEA, Grenoble INP, IRIG, PHELIQS, 17 av. des Martyrs, 38000 Grenoble, France*
[3] *Univ. Grenoble-Alpes, CNRS, Institut Néel, 25 av. des Martyrs, 38000 Grenoble, France*
[4] *Univ. Grenoble-Alpes, CEA, LETI, 17 av. des Martyrs, 38000 Grenoble, France*
[*] *eva.monroy@cea.fr*

**Abstract:** We report net gain measurements at room temperature in $Al_{0.07}Ga_{0.93}N$/GaN 10-period multi-quantum well layers emitting at 367 nm, using the variable stripe length method. The separate confinement heterostructure was designed targeting electron-beam pumped lasing at 10 kV. The highest net gain value was 131 $cm^{-1}$, obtained at the maximum pumping power density of the experimental setup (743 kW/$cm^2$). The net gain threshold was attained at 218 kW/$cm^2$ using 193 nm optical pumping. From these experiments, we predict an electron-beam-pumped lasing threshold of 370 kW/$cm^2$ at room temperature, which is compatible with the use of compact cathodes (e.g. carbon nanotubes). In some areas of the sample, we observed an anomalous amplification of the photoluminescence intensity that occurs for long stripe lengths (superior to 400 µm) and high pumping power (superior to 550 kW/$cm^2$), leading to an overestimation of the net gain value. We attribute such a phenomenon to the optical feedback provided by the reflection from cracks, which were created during the epitaxial growth due to the strong lattice mismatch between different layers.

© 2022 Optica Publishing Group under the terms of the Optica Open Access Publishing Agreement

## 1. Introduction

Ultraviolet (UV) lasers find application in many domains, such as micromachining, polymer curing, gas analytics, disinfection, microsurgery and medical treatments, as well as in Lidar remote detection and non-line-of-sight (NLOS) communication [1, 2]. The demand on UV lasers is currently covered by excimer lasers (ArF, $Ar_2$, XeCl, . . . ) and lasers based on frequency conversion (Nd:YAG). These lasers come with several regulations and specific safety instructions: For example, toxic gases are involved in the operation of excimer lasers, in both the injection phase ($F_2$, Xe, . . . .) and the lasing phase, with the release of $O_3$ as the by-product of the gas ionization process. Frequency-conversion lasers rely on non-linear processes to operate in UV wavelength range, which often have to deal with stability issues and the ageing of optics, with some being highly hygroscopic. Wide band-gap semiconductors, like AlGaN alloys, could provide an alternative for electrically injected UV lasers. However, the requirement of low resistivity and high hole concentration for p-type AlGaN poses a challenge for the development of laser diodes, which results in an important increase of the lasing threshold for devices emitting at wavelengths shorter than 365 nm [3]. Furthermore, the short diffusion length of holes limits the size of the active region, since recombination takes place only in the quantum wells (QWs) closer to the p-type region.

Recently, electron beam pumping was proposed as an alternative solution to inject electrons and holes into the AlGaN based active region [4], obviating the need for p-type AlGaN. In

#454381 https://doi.org/10.1364/OE.454381
Journal © 2022 Received 20 Jan 2022; revised 27 Apr 2022; accepted 30 Apr 2022; published 28 Jun 2022

this approach, high-energy electrons are first accelerated from a cathode to the sample, and then transmit their kinetic energy to valence band electrons via impact-ionization processes, generating electron-hole pairs. Electrons and holes are injected with equal spatial distribution in the semiconductor, and the injection depth can be tuned through the accelerating voltage to match the thickness of the active medium. Experimental demonstrations of UV lasing with this method were reported by Hayashi *et al.* ($Al_{0.07}Ga_{0.93}N$/GaN multi-quantum well (MQW) displaying a lasing threshold of 230 kW/cm2 at 107 K [5]) and by Wunderer *et al.* (InGaN QWs in a GaN/AlGaN separate confinement heterostructure, displaying a lasing threshold of 159 kW/cm$^2$ at 77 K [6]). It is therefore interesting to conduct further experiments on this kind of structures, like a quantification of the net optical gain, seeking operation at room temperature and a comparison with AlGaN-based laser diodes.

Here, we present measurements of net optical gain at room temperature in an $Al_{0.07}Ga_{0.93}N$/GaN MQW, using the variable stripe length (VSL) method [7]. The MQW is embedded in an $Al_{0.15}Ga_{0.85}N/Al_{0.07}Ga_{0.93}N$ separate confinement heterostructure (SCH), designed for electron-beam pumping at 10 kV [8]. The structure of the sample resembles closely the one described in Ref. [5] for the demonstration of an electron-beam pumped laser. Gain measurements were conducted at two different positions in the sample. The results depend on the probed position, with the net gain threshold observed between 218 kW/cm$^2$ and 403 kW/cm$^2$. At the position with higher net gain threshold (403 kW/cm$^2$), we observed an anomalous amplification of the photoluminescence (PL) intensity, which occurs at long stripe lengths (superior to 400 µm) and high pumping power (superior to 550 kW/cm$^2$). We attribute this phenomenon to the optical feedback provided by reflection at cracks, which were formed during the epitaxial growth, due to the strong lattice mismatch between the SCH and the GaN substrate. Combining the net gain results and the intrinsic efficiency limit of electron beam pumping process, we predict a lower limit of 370 kW/cm$^2$ for electron beam pumped laser threshold at room temperature for this structure.

## 2. Sample and experimental setup

The sample under study consists of a 10-period $Al_{0.07}Ga_{0.93}N$/GaN MQW, sandwiched between two layers of $Al_{0.07}Ga_{0.93}N$ as top/bottom inner claddings, and two layers of $Al_{0.15}Ga_{0.85}N$ as top/bottom outer claddings, all grown on top of a bulk GaN substrate using plasma-assisted molecular beam epitaxy (MBE). Note that this is a different growth approach with respect to Ref. [5], where the structure was grown by metalorganic vapor phase epitaxy (MOVPE). Both growth techniques have demonstrated their capacity to synthesize AlGaN-based UV emitters [9–14]. Although not as extensively used as MOVPE, MBE presents some advantages in terms of interface control, memory effects and defect incorporation, due to its comparatively low growth temperature.

A schematic of the sample is presented in Fig. 1(a). The detailed growth conditions can be found in Ref. [15]. The layer thicknesses of the $Al_{0.07}Ga_{0.93}N$/GaN MQW (11.4 nm $Al_{0.07}Ga_{0.93}N$/ 2.8 nm GaN) are very similar to those used by Hayashi *et al.* (nominally 12 nm $Al_{0.07}Ga_{0.93}N$/ 3 nm GaN) for the demonstration of UV lasing under electron beam pumping [5]. However, the waveguide was modified, aiming to reduce the required accelerating voltage and increase the optical confinement factor in the MQW [8]. We depict, in Fig. 1(b), Monte Carlo simulations (CASINO software) of the electron-hole pair generation profile under electron beam pumping with acceleration voltages $V_a$ = 7 kV and $V_a$ = 10 kV. The location of the waveguide core relative to the surface (i.e. the thickness of the top cladding layer) is chosen to enhance the carrier generation and collection in the active area. Note that the generation profile is very different in the case of laser pumping, also shown in the figure (calculation using the absorption coefficients reported by Muth *et al.* [16]). In this latter case, carriers are generated mostly in the top cladding layer and they have to diffuse to the MQW. In the same figure, we also display the optical field

Optics EXPRESS

distribution in the first optical mode confined in the heterostructure, obtained from commercial finite-element analysis software (Comsol Multiphysics). The values of refractive indices were taken from Refs. [17,18]. The asymmetry of the guided mode is due to the non-symmetric refractive index profile of the active layer. The location of the MQW within the waveguide core is intended to improve the overlap with the optical mode. From the calculation, the optical confinement factor is estimated about 7% (to be compared with about 6% in the original design of Hayashi *et al.* [5]).

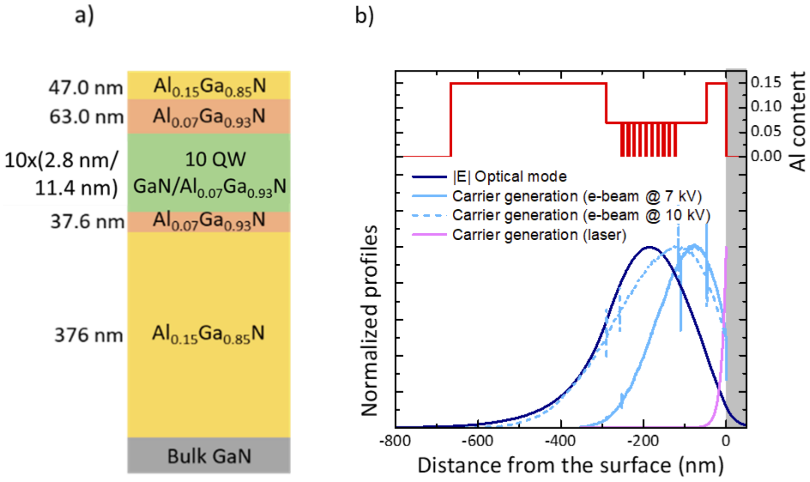


**Fig. 1.** a) Schema of the $Al_{0.07}Ga_{0.93}N$/GaN MQW structure under study. b) Simulation of the optical field distribution in the first optical mode, together with calculations of the carrier generation as a function of depth, normalized to its maximum, in the cases of pumping with an electron beam (acceleration voltages $V_a$ = 7 kV and $V_a$ = 10 kV) or with a UV laser (wavelength $\lambda = 193$ nm).

The periodicity of the MQW was analyzed by a high-resolution X-ray diffraction (HRXRD) in a Rigaku SmartLab diffractometer. A $\theta - 2\theta$ X-ray scan around the (0002) reflection of GaN is presented in Fig. 2(a), and a reciprocal space map around the (10-15) reflection is presented in Fig. 2(b). In the reciprocal space map, we can identify the reflection from the $Al_{0.15}Ga_{0.85}N$ claddings, whose location confirms that the Al mole fraction is $0.150 \pm 0.005$ and the layer is partially relaxed. The reflection of $Al_{0.15}Ga_{0.85}N$ and the satellites of the MQW are vertically aligned, which confirms that the MQW grows pseudomorphically on the bottom cladding. The experimental diffractogram in Fig. 2(a) is displayed together with a theoretical calculation based on the structure shown in Fig. 1(a) assuming that the $Al_{0.15}Ga_{0.85}N$ bottom cladding is 50% relaxed. There is an excellent agreement between experiment and calculation.

Additional structural studies were conducted using bright-field transmission electron microscopy (TEM) performed on a FEI Thémis microscope operated at 200 kV. A TEM image of 3 QWs in the center of the MQW is presented in Fig. 2(c). It shows well-defined planar interfaces. TEM provides a local measurement of the layer thickness, in contrast with the HRXRD measurements that provide the average thickness in a several-millimeter-squared area. The layer thicknesses listed in Fig. 1(a) are within the error bars of the measurements in Fig. 2(c), indicated in monolayers (1 monolayer is 1 ML ≈ 0.26 nm).

The optical performance of the sample was tested by cathodoluminescence (CL) spectroscopy as a function of the acceleration voltage. Measurements were carried out in a FEI Inspect F50 scanning electron microscope equipped with an iHR550 spectrometer and an Andor Technology Newton DU940 BU2 spectroscopic charge-coupled device (CCD) camera. The beam spot

Optics EXPRESS

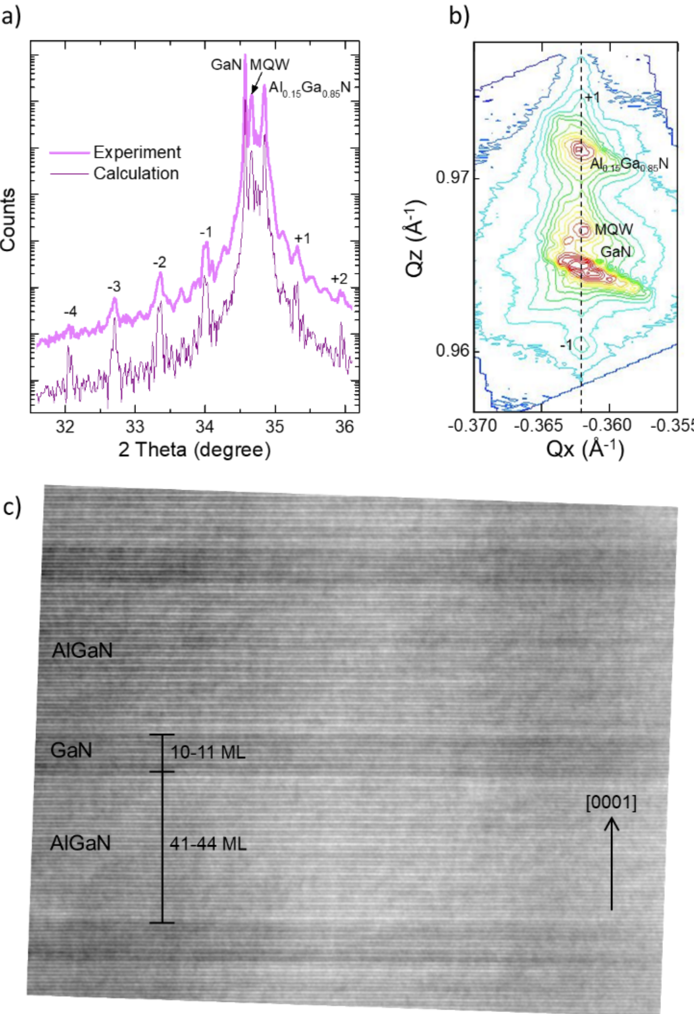


**Fig. 2.** a) HRXRD $\theta - 2\theta$ scan around the (0002) reflection of GaN, together with a theoretical calculation for the structure shown in Fig. 1(a), assuming 50% relaxation of the $Al_{0.15}Ga_{0.85}N$ bottom outer cladding layer. Labels indicate the original diffraction peaks of the bulk GaN substrate, the $Al_{0.15}Ga_{0.85}N$ layers and the $Al_{0.07}Ga_{0.93}N$/GaN MQW, along with the order of its satellite peaks. b) Reciprocal space map around the (10-15) reflection of GaN, showing that the MQW grows pseudomorphic on the $Al_{0.15}Ga_{0.85}N$ layer (same in-plane reciprocal vector, $Q_x = -2/\left(a\sqrt{3}\right)$, where $a$ is the in-plane lattice parameter). Note that for this reflection, the out of plane reciprocal vector is $Q_z = 1/(5c)$, where $c$ is the out-of-plane lattice parameter. c) Bright-field TEM image of three QWs in the active region, showing the well/barrier thickness and the sharpness of the heterointerfaces.

Optics EXPRESS

diameter was ≈ 10 nm on the focal point, the scanning area was a square of 4 μm$^2$, the accelerating voltage was varied from $V_a$ = 5 kV to 20 kV and the injection current was around 100 to 150 pA. The CL was collected from the top of the as-grown sample at room temperature.

CL results are presented in Fig. 3. The dominant peak around 360 nm correspond to emission from the MQW and the shoulder around 350 nm is due to recombination in the $Al_{0.07}Ga_{0.93}N$ layers. Let us remind here that increasing $V_a$ results in an increase of the penetration depth of the injected electrons, as it is observed in Fig. 1(b) when comparing the carrier generation as a function of depth for $V_a$ = 7 kV and $V_a$ = 10 kV. From Fig. 3, the efficiency of the MQW emission remains almost constant when varying the acceleration voltage up to 7 kV. At this moment, looking back to Fig. 1(b), maximum generation takes place at the topmost $Al_{0.07}Ga_{0.93}N$ layer, and the generation area is contained within the core of the waveguide. This means that the diffusion of carriers from the topmost layers of the waveguide to the MQW is an efficient process. However, the efficiency decreases progressively when increasing the acceleration voltage from 7 to 10 kV, i.e. when the electron beam penetrates the $Al_{0.15}Ga_{0.85}N$ bottom cladding layer of the waveguide. This is consistent with our previous calculations of the band diagram in this kind of SCH [8], which showed that the different polarization along the heterostructure results in a band bending that behaves as a potential barrier for carrier diffusion at the bottom $Al_{0.07}Ga_{0.93}N/Al_{0.15}Ga_{0.85}N$ interface.

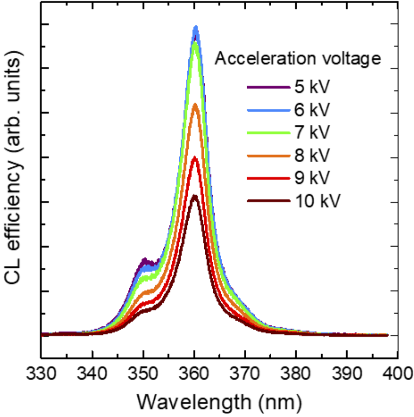


**Fig. 3.** Room temperature CL efficiency spectra measured at various acceleration voltages. To obtain the CL efficiency, raw intensity values were divided by the injected current and acceleration voltage.

We conducted net gain measurements at room temperature, using the VSL method described in Ref. [7], with the experimental setup illustrated in Fig. 4. The pump source was a 193 nm ArF excimer laser (Compex 102 from Coherent), operated in pulse mode (20 ns pulse width, with a frequency capped at 20 Hz). Such pump laser was already used in several studies of optical gain in AlGaN-based MQW [19–21]. Since the ArF laser beam dimension is relatively large (10 mm × 24 mm), to create a narrow laser stripe on the sample, we insert a rectangular slit (0.05 mm × 3 mm) in front of the laser beam, then recreate its image on the sample using two fused silica spherical lens. The laser stripe on the sample has a width of 25 μm and a maximum length of 1500 μm. A mobile shutter is positioned in front of the sample to modify the stripe length. Both the sample and the laser stripe can be imaged by reflection on a CMOS camera (Thorlabs DCC1240M). The beam intensity can be modified using fused silica reflective optical densities. PL signals are collected using an optical fiber and then analyzed with a Horiba Triax 320 spectrometer (grating of 1200 grooves/mm, with blaze wavelength at 330 nm), coupled with a cooled CCD camera (Symphony STE).

Optics EXPRESS

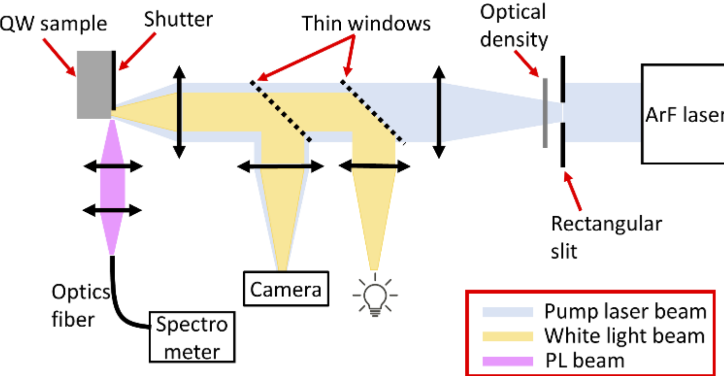


**Fig. 4.** Experimental setup for net gain measurements using the VSL method.

To perform the VSL measurements, one of the edges of the sample was mechanically cleaved along the *m*-plane of the GaN substrate, to provide a clean output facet. The lateral confinement of light is obtained by gain guiding, i.e. by the fact that the population-inverted region is determined by the width of the pumping laser stripe, which generates a gain gradient in the structure. To study the homogeneity of the sample, we performed gain measurements on two different areas, denoted as position 1 and position 2 hereinafter.

At the laser wavelength (193 nm), the penetration of the laser beam, i.e. the photogeneration of carriers, is described by the magenta curve in Fig. 1(b). This means that 90% of the pumping power is absorbed in the topmost 77 nm of the sample. Photogenerated carriers can thermalize and diffuse to the active MQW to contribute to the emission. The analysis of the CL data in Fig. 3 shows that the carrier diffusion from the topmost layers is an efficient process. However, this leads to an uneven distribution of carriers within the 10 QWs, i.e. the carrier density in the wells close to the surface is much higher than that in the deeper wells. As a result, higher pumping densities are required to attain the lasing threshold since the QWs that do not reach the population inversion contribute to increase the absorption loses, and there might be some additional losses due to surface recombination. Let us remind here that the design of the active region is not optimized for optical pumping but for electron beam pumping. Optimizing the structure for optical pumping would imply less QWs in the active region, and located closer to the surface. Keeping all this in mind, the gain measurements extracted through the VLS method using optical pumping are valid, which is the main focus of this work, but the lasing threshold values obtained from such measurements are certainly overestimated.

## 3. Results

Figures 5(a) and (b) describe the PL spectra recorded at positions 1 and 2, respectively, measured with a pumping power of 743 kW/cm$^2$, as a function of the stripe length between 40 µm and 400 µm. At position 1 (Fig. 5(a)), the PL intensity increases systematically as the stripe length increases, with the highest signal observed for a length of 400 µm. At position 2 (Fig. 5(b)), the behavior is similar for stripes shorter than 240 µm. Then, the PL intensity increases rapidly in the range of 240-360 µm, and the shape and width of the PL peak changes. Finally, for the 400 µm long stripe, the intensity saturates. The evolution of the full width at half maximum (FWHM) of the PL peak is shown in Fig. 5(c). For stripes longer than 240 µm, the FWHM at position 2 becomes narrower than that at position 1, decreasing down to 1.5 nm at position 2 compared to 2.6 nm at position 1. The superlinear increase of the PL intensity with the stripe length, along with the spectral narrowing, confirm the presence of amplified spontaneous emission (ASE).

Research Article Vol. 30, No. 14 / 4 Jul 2022 / Optics Express 25225


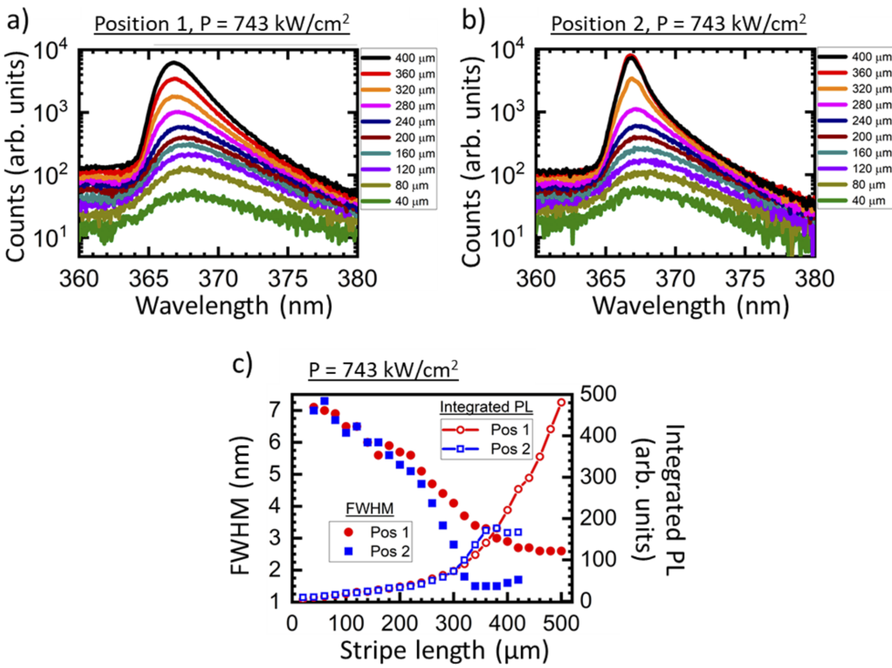


**Fig. 5.** PL spectra obtained from the $Al_{0.07}Ga_{0.93}N$/GaN MQW structure for different stripe lengths, at (a) position 1 and (b) position 2. The stripe lengths are indicated in the legends. (c) PL peak FWHM at position 1 and position 2 and integrated PL intensity as a function of the stripe length.

In the VSL method [7], the variation of the PL intensity $I_\lambda$ at a certain wavelength $\lambda$, as a function of the stripe length $l$, is described by a one-dimensional optical amplifier model:

$$I_\lambda(l) = \frac{I_s A}{g_\lambda}(e^{g_\lambda l} - 1) \tag{1}$$

where $I_s$, $A$, $g_\lambda$ are the spontaneous emission rate per unit volume, the cross-section area of the excited volume and the net gain at $\lambda$, respectively. By plotting $I_\lambda(l)$ and then fitting it with equation (1), we can extract the optical net gain $g_\lambda$.

Figure 6(a) shows, for the position 1, the evolution of the PL intensity at $\lambda = 367$ nm as a function of the stripe length, for several values of pumping power between 218 kW/cm$^2$ and 743 kW/cm$^2$ (indicated in the figure panels). The fitted net gain varies from –24 cm$^{-1}$ (absorption) at 218 kW/cm$^2$, up to 129 cm$^{-1}$ at 743 kW/cm$^2$. The curve shape is different between the case of absorption, where the signal starts to saturate at long stripe length, and in the case of net gain, with an exponential-like increase of the PL intensity. By repeating the fitting process at different wavelengths, we plot, in Fig. 6(b), the net gain as a function of wavelength and pumping power. Positive net gain exists for pumping power higher than 218 kW/cm$^2$, with the highest net gain equal to 131 cm$^{-1}$ ($\lambda = 366.5$ nm) for a pumping power of 743 kW/cm$^2$. At 218 kW/cm$^2$, net gain still exists, but with very low values (3.1 cm$^{-1}$ at $\lambda = 361$ nm). The peak net gain blue shifts from 371 nm at 218 kW/cm$^2$ to 366.5 nm at 743 kW/cm$^2$, as expected due to band filling. At longer wavelengths, the net gain becomes negative as absorption internal loss dominates. We have decided to limit the spectra to 375 nm on the long wavelength side since the reduced PL intensity results in poor signal-to-noise ratio. On the other hand, the response observed for wavelengths shorter than 365 nm might stem from the mixed optical response of the top claddings (47 nm thick $Al_{0.15}Ga_{0.85}N$ layer and 63 nm thick $Al_{0.07}Ga_{0.93}N$ layer) and the MQW.

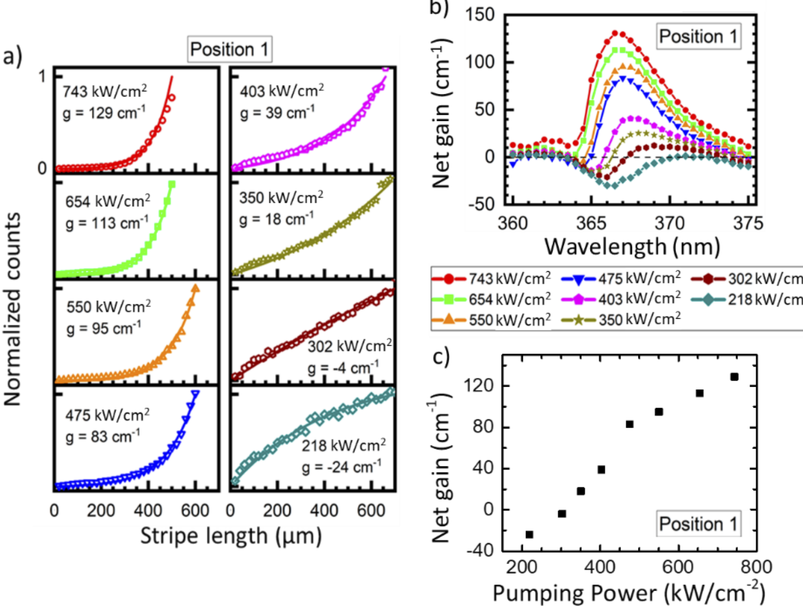


**Fig. 6.** Net gain measurements performed at position 1: a) PL intensity at $\lambda = 367$ nm, as a function of the stripe length, for pumping power between 218 kW/cm$^2$ and 743 kW/cm$^2$. Raw data are presented as symbols and fits are presented as solid lines. The pumping power and the gain value extracted from the fit are shown in each corresponding graph. b) Net gain as a function of wavelength, for pumping power between 218 kW/cm$^2$ and 743 kW.cm$^{-2}$. Positive values indicate the presence of net gain, while negative values indicate absorption. c) Variation of the maximum net gain as a function of the pumping power.

To compare these results with the literature, we have compared the maximum reported net gain divided by the number of QWs in the structure. Assuming that all the QWs are active, the maximum net gain obtained here is 13 cm$^{-1}$/QW, in line with results in the literature, in the range of 12-15 cm$^{-1}$/QW [22–25]. However, we are aware that the comparison of gain values is difficult, since the designs have different thicknesses, number of QWs or Al composition. The carrier density in the wells depend on the carrier diffusion process, so that most probably only the topmost QWs reach population inversion, meaning that we are underestimating the real gain by dividing by the total number of QWs. In addition, representing the net gain as a function of the pumping power in Fig. 6(c), we observe that gain saturation is not reached yet at the highest pumping power used in this experiment, so that the maximum net gain for this structure might be slightly higher.

We repeated the same net gain measurement at position 2. Compared to position 1, here, at high pumping powers, the PL intensity at 367 nm shows a sharper increase followed by a saturation at high values of stripe length (Fig. 7(a), measurements at 654 kW/cm$^2$ and 743 kW/cm$^2$). The saturation part of the graphs was excluded (if present) during the fit process to extract the gain. The net gain curves as a function of wavelength and pumping power are plotted in Fig. 7(b). In this position, the net gain threshold is 403 kW/cm$^2$, higher than that at position 1 (218 kW/cm$^2$). However, the maximum net gain at 743 kW/cm$^2$ is 240 cm$^{-1}$, significantly higher than that at position 1 (131 cm$^{-1}$). The shape of the curve changes for the three highest pumping powers (550 kW/cm$^{-2}$, 654 kW/cm$^2$ and 743 kW/cm$^2$), resembling a peak rather than the rounded profile expected in net gain measurements.

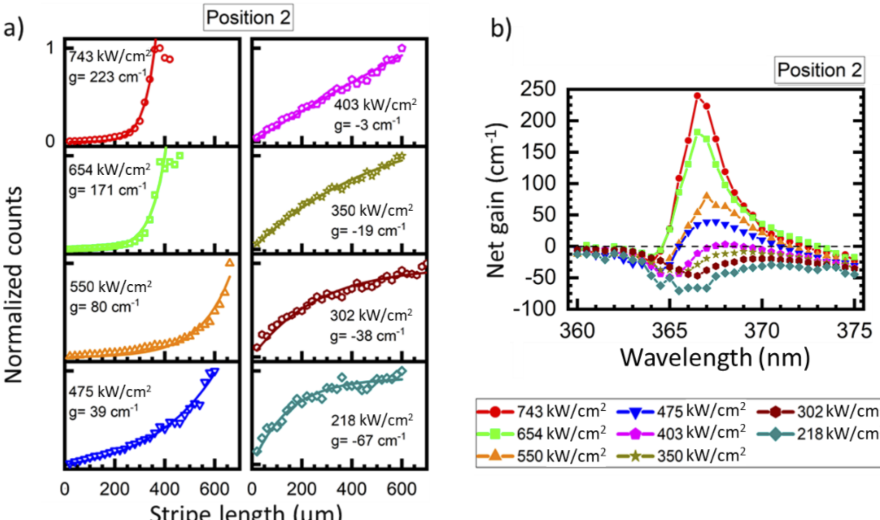


**Fig. 7.** Net gain measurements performed at position 2: a) PL intensity at λ= 367 nm, as a function of stripe length, for pumping power between 218 kW/cm$^2$ and 743 kW/cm$^2$. Raw data are presented as symbols and fits are presented as solid lines. b) Net gain as a function of wavelength, for pumping power between 218 kW/cm$^2$ and 743 kW/cm$^2$.

## 4. Discussion

### 4.1. Validity of Eq. (1)

The validity of Eq. (1) relies on several assumptions. First, we assume a constant gain coefficient along the stripe. This condition is not verified in the case of gain saturation, which occurs when the ASE intensity induces a depletion of carriers in the excited state, as the PL intensity builds up along the stripe [26]. Such a phenomenon can create a saturation of PL intensity at long stripes, as observed in position 2 for stripe lengths longer than 400 µm and pumping power higher than 600 kW/cm$^2$ (Fig. 7(a)), which must therefore be excluded in the gain fitting process with Eq. (1).

In theory, a saturation-like effect could also be obtained in a configuration where the longest stripes reach an area with lower crystal quality, i.e. lower optical gain. However, we do not expect such an effect in our samples. These structures were grown on bulk GaN substrates, with a nominal dislocation density below 10$^8$ cm$^{-2}$, which means that the average distance between dislocations is in the range of 1 µm. In TEM images, these defects appear randomly distributed (see Fig. 8), so that they should not introduce a variation of the signal as a function of length in measurements that are in the hundreds-of-µm range. On such a length scale, there might be a thermal gradient during the growth that could lead to a compositional drift in the AlGaN alloy. However, x-ray measurements look homogenous along the samples (about 2-3 cm$^2$) in terms of thickness and composition (the thickness variation across the sample is below 5%). In summary, we do not expect significant structural inhomogeneities along the laser stripe. In addition to these arguments, the saturation effect in Fig. 6(a) is only observed for the two higher pumping powers, whereas an abrupt structural degradation should also have affected low power measurements.

Second, as discussed in Ref. [26], at low pumping power, the weaker gain gradient and pump-induced refractive index gradient can generate a larger optical mode spreading into the unexcited area of the sample. In this case, inhomogeneous coupling of PL signal can take place, affecting the light collection efficiency and introducing error in the calculation of gain, which is particularly critical near the net gain threshold (here, around 218 kW/cm$^2$). However, all pumping powers in this study remain in the range of hundreds of kW/cm$^2$, i.e. in the high regime of optical

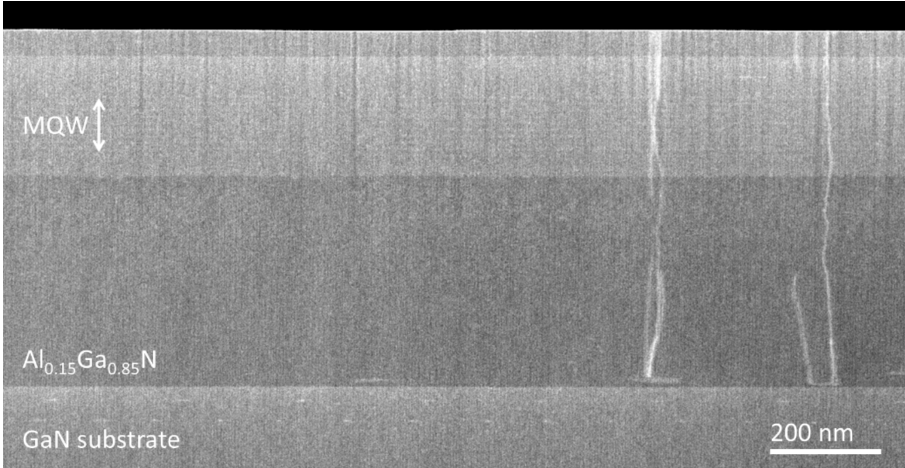


**Fig. 8.** High-angle annular dark field scanning transmission microscopy image of an AlGaN/GaN SCH grown on bulk GaN. Some dislocations appear as vertical white lines.

excitation, and thus maintain a sufficiently strong guiding effect to validate the one-dimensional optical amplifier model, described by the Eq. (1). Therefore, the error in gain values related to this effect should be minimal.

### 4.2. Difference between position 1 and position 2

There are several important differences between the results at positions 1 and 2. The maximum net gain at 743 kW/cm$^2$ is higher at position 2, but the spectral distribution of the gain is unusual, the PL emission is particularly narrow and there is evidence of gain saturation at long stripe lengths. To understand the mechanisms behind this optical response, we analyzed the evolution of the emission characteristics (intensity and FWHM) as a function of the pumping power for a fixed stripe length, namely 400 μm, which already shows different behavior at positions 1 and 2. Results for both positions are presented in Fig. 9(a)-(b). The response is similar for pumping power lower than 550 kW/cm$^2$. At higher pumping power, for position 2, there is a larger superlinear enhancement of the PL intensity, with a collapse of the FWHM. Together, these features suggest the onset of lasing, which would be expected for a material with gain within an optical cavity, but it is not expected in a sample with only one cleaved facet. However, the image of our sample under an optical microscope (see Fig. 9(c)) reveals the presence of very straight cracks that propagate along the *m*-planes: they appear parallel to the cleaved edge and also forming a 60° angle. These cracks are generated in AlGaN layers grown under tensile stress, as it is the case here due to the lattice mismatch with the GaN substrate. Partial reflection from cracks parallel to the cleaved edge could provide the optical cavity feedback that amplifies the PL intensity, resulting in the anomalous behavior of the emission characteristics observed at position 2. In this case, care must be taken for the interpretation of net gain using the Eq. (1), since the effective stripe length might increase due to multiple round trips of photons between a crack and the cleaved edge.

Due to the interaction between cracks, the distance between the cleaved edge and the first crack is not constant along the sample, e.g. it is around 300 μm in the lower part of Fig. 9(c), and around 600 μm in the upper part of the image. This length scales are comparable with our maximum stripe length, which explains the different behavior in different areas of the sample. Thus, we can conclude that position 1 has the typical behavior expected in a reliable net gain

Optics EXPRESS

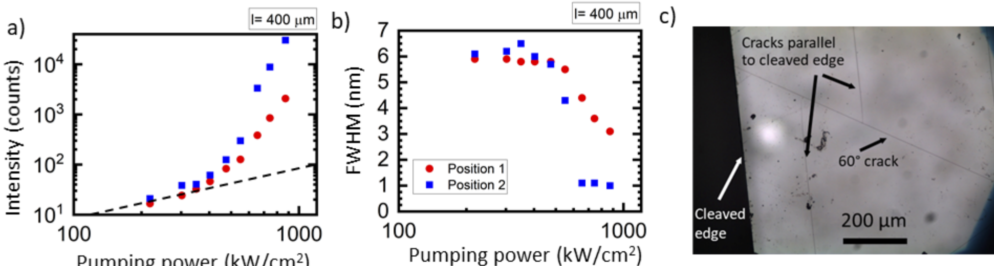


**Fig. 9.** Variation of (a) the PL intensity and (b) the PL peak FWHM as a function of the pumping power measured at position 1 and position 2, for a stripe length of 400 μm. The dashed line in (a) indicates the slope that corresponds to a linear trend. (c) Top view of the sample in the proximity of the cleaved edge. Cracks propagate either parallel to the cleaved edge or forming an angle of 60°.

measurement, whereas position 2 presents an amplification of the response for long stripes due to the optical feedback provided by a crack.

Changing the measurement point in the sample, we observe locations with the behavior of positions 1 and 2. The high density of cracks makes that domains with the response described as "position 2" are relatively dominant. Attempts to perform similar measurements in samples emitting at shorter wavelengths (designs emitting at 355 nm in Ref. [8]) encountered higher difficulties: it was hardly possible to find spots without optical amplification due to the shorter distance between cracks originated by the higher misfit strain. Therefore, gain measurements were systematically overestimated. Solving this issue would require advanced strain management during the growth process, either growing on patterned substrates or on bulk AlN. However, for these emission wavelengths, AlN substrates present a higher lattice mismatch than GaN. The resulting strain in the structure is compressive, which favors relaxation by dislocations (instead of crack propagation for tensile strain).

The presence of cracks is not catastrophic for the device performance: The distance between cracks is large enough to allow the fabrication of devices, and we have demonstrated that they do not have a significant role once the second facet of a laser bar is cleaved, even in millimeter-long cavities. Characterization results of laser bars fabricated from the sample reported here were discussed in Ref. [27].

### 4.3. Comparison with literature

To compare the lasing threshold of different structures, we must keep in mind that the gain depends not only on the pumping procedure but also on the number of QWs. Therefore, to take this factor in to account, we will also compare the carrier density per QW at the threshold, $N_{th}$. This parameter is in the range of state-of-the-art of UV laser diodes based on an SCH (see Table 1 and Fig. 10). A reduction of $N_{th}$ can be obtained by modifying the structure to be specifically adapted for optical pumping, approaching the QWs to the surface [28–30]. However, such designs are not compatible with electron beam pumping.

### 4.4. Estimation of the lasing threshold under electron beam pumping

In the case of an optical cavity with very low mirror losses (for example in very long Fabry-Perot cavities), the presence of optical net gain can be used as an indicator to estimate the threshold power required for lasing under electron beam pumping. To compare lasing thresholds measured with different types of carrier injection in the same active region, i.e. optical pumping, electrical injection or electron beam pumping, we estimate their energy cost to achieve the same carrier

Optics EXPRESS

**Table 1. Reported values of lasing wavelength (λ), threshold current ($I_{th}$) or threshold power density ($P_{th}$) at room temperature and surface carrier density ($N_{th}$) injected per QW and per second at the lasing threshold for several UV laser diodes. The active region structure (MQW = multi-quantum well, SQW = single quantum well) and heterostructure design are also indicated.**

| Ref. | Year | λ (nm) | $I_{th}$ (kA/cm$^2$) | $P_{th}$ (kW/cm$^2$) | $N_{th}$ per QW (×10$^{22}$ s$^{-1}$cm$^{-2}$) | Active region | Heterostructure design |
|---|---|---|---|---|---|---|---|
| [31] | 2009 | 354.4 - 359.6 | 8 | – – | 1.7[a] | GaN/AlGaN MQW | SCH, 5 µm ridge, 500 µm cavity |
| | | 336.0 - 342.3 | 17.6 | – – | 3.7[a] | AlGaN/AlGaN MQW | SCH, 5 µm ridge, 500 µm cavity |
| [32] | 2008 | 355.4 - 361.6 | 19.1 ± 5.5 | — | 4 | 3 × GaN/AlGaN | SCH, 5 µm ridge, 1000 µm cavity |
| [33] | 2004 | 365 | 3.5-4.5 | – | 0.83[a] | 2-7 × GaN/AlGaN | SCH, 2 µm ridge, 500 µm cavity |
| [34] | 2001 | 366.9 | 3.5 | – | 2.2 | SQW GaN/AlGaN | SCH, 2.5 µm ridge, 600 µm cavity |
| [35] | 2020 | 278.9 | 19.6 | — | 12.3 | SQW AlGaN/AlGaN | SCH, 4 µm ridge, 400 µm cavity, $HfO_2/Al_2O_3$ DBR |
| [36] | 2019 | 271.8 | 25 | – | 15.5 | SQW AlGaN/AlGaN | SCH, 4 µm ridge, 400 µm cavity $HfO_2/SiO_2$ DBR |
| [37] | 2007 | 355.4 - 361.6 | 19.1 ± 5.5 | – | 4 | 3 × GaN/AlGaN | SCH, 5 µm ridge, 1000 µm cavity |
| [38] | 2021 | 300 | 14.2 | – | 4.4 | 2 × AlGaN/AlGaN | SCH, 10 µm ridge, 2000 µm cavity |
| [39] | 2015 | 350 | 56 | – | 11.7[a] | GaN/AlGaN MQW | SCH, 1.5 µm ridge, 300 µm cavity |
| [40] | 2020 | 298 | 41 | – | 25.6 | SQW AlGaN/AlGaN | SCH, 300 µm cavity |
| [41] | 2004 | 350.9 | 7.3 | – | 1.5 | 3 × GaN/AlGaN | SCH, 5.5 µm ridge, 500 µm cavity |
| [42] | 2012 | 267 | – | 126 | 5.2[b] | 3 × AlGaN/AlGaN | SCH, 160 µm ridge, 1 mm cavity |
| [28] | 2018 | 267 | – | 6 | 0.2[b] | 3×AlGaN/AlGaN | QWs at the surface |
| [29] | 2019 | 245 | – | 190 | 0.5[b] | 40×GaN/AlGaN | QWs at the surface |
| [30] | 2014 | 256 | – | 61 | 1.2[b] | 5×AlGaN/AlGaN | QWs at the surface |
| This work | 2022 | 367 | – | 218 | 2.1[b] | 10 × GaN/AlGaN | SCH designed for electron beam pumping, 50 µm ridge, 1 mm cavity |

[a] $N_{th}$ per QW estimated assuming 3 active QWs.
[b] $N_{th}$ per QW estimated as the photon flux divided by the number of QWs, considering the optical pumping wavelength.

Optics EXPRESS

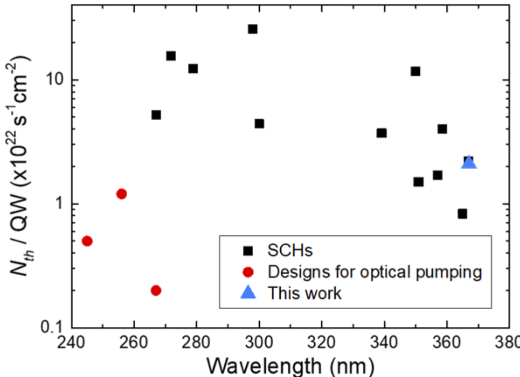


**Fig. 10.** Variation of $N_{th}$ per QW as a function of the emission wavelength (data from Table 1). Data corresponding to SCHs and heterostructures optimized for optical pumping are represented with different symbols and colors.

density threshold. In this work, under optical pumping with an ArF laser (λ = 193 nm), the energy cost to generate an electron-hole pair is the laser photon energy, $E_{laser}$ = 6.42 eV. In the case of electron beam pumping, the energy required to generate an electron-hole pair is about 3 times the band gap [43], i.e. $E_{ebeam} \approx 3 \times 3.6$ eV = 10.8 eV. With this data, the threshold for electron beam pumping, $P_{th}^{ebeam}$, can be estimated from the optical threshold, $P_{th}^{laser}$, using

$$P_{th}^{ebeam} = \frac{E_{ebeam}}{E_{laser}} P_{th}^{laser} \quad (2)$$

For the SCH design studied in this work, with a net gain threshold of 218 kW/cm$^2$, we estimate a lasing threshold $P_{th}^{ebeam} \approx$ 370 kW/cm$^2$ under electron beam pumping at room temperature. However, it should be kept in mind that the net gain threshold obtained in this work is overestimated, since measurements were performed by optical pumping, meaning that only the topmost QWs are expected to attain population inversion, and the others contribute to enhance the absorption losses. Therefore, the calculated lasing threshold is indeed an upper limit.

## 5. Conclusion

We reported optical net gain measurements at room temperature in an SCH containing a 10-period $Al_{0.07}Ga_{0.93}N$/GaN MQW emitting at 367 nm. In this paper, we described the challenge of performing optical net gain measurements in an SCH designed for electron beam pumping. Due to the electron penetration profile, such structures can host multiple QWs within a hundred-of-nm thick active region. This is a major difference with respect to laser diodes or optically pumped lasers, where the optimum number of QWs is typically 1-2, due to the low diffusion length of holes in III-nitrides. In structures designed for electron beam pumping, characterizing gain by optical pumping is complex, since optical excitation is restricted to the proximity of the surface and only the topmost QWs can attain population inversion. In spite of these limitations, the results presented here are at the state of the art. The net gain threshold was found at 218 kW/cm$^2$, and a net gain value of 131 cm$^{-1}$ was obtained at a pumping power of 743 kW/cm$^2$. By combining the net gain threshold with the theoretical limit of electron-hole generation efficiency in the cathodoluminescence process, we predict, for this structure, a lasing threshold around 370 kW/cm$^2$ for the electron beam pumping at room temperature.

Interestingly, in some areas of the sample, we observed an anomalous amplification that occurs for long stripe lengths (superior to 400 µm) and high pumping powers (superior to 550 kW/cm$^2$) at the position with higher net gain threshold. We attributed this phenomenon to the

Optics EXPRESS

optical feedback provided by reflection at cracks, which appear due to plastic relaxation of misfit strain in AlGaN-based structures grown on GaN substrates. The propagation of cracks is a common relaxation process in III-nitride heterostructures grown under tensile stress, and it is not catastrophic for the device performance. However, they can induce an overestimation of the gain measurements, which can be identified from the spectral variation of the gain. We consider that this information can be relevant for the interpretation of gain measurements, particularly when working with lattice-mismatched heterostructures.

**Funding.** Région Auvergne-Rhône-Alpes (PEAPLE); Agence Nationale de la Recherche (ANR-18-CE24-0014).

**Acknowledgements.** The authors would like to thank the platform PLYRA of Institut Lumière Matière - University Claude Bernard Lyon 1 for their support of scientific equipment during this work.

**Disclosures.** The authors declare no conflicts of interest.

**Data availability.** Data underlying the results presented in this paper are not publicly available at this time but may be obtained from the authors upon reasonable request.

## References

1. D. J. Elliott, *Ultraviolet Laser Technology and Applications* (Academic Press, 1995).
2. M. Kneissl and J. Rass, eds., *III-Nitride Ultraviolet Emitters: Technology and Applications*, 1st ed. 2016, Springer Series in Materials Science No. 227 (Springer International Publishing : Imprint: Springer, 2016).
3. H. Amano, R. Collazo, C. D. Santi, S. Einfeldt, M. Funato, J. Glaab, S. Hagedorn, A. Hirano, H. Hirayama, R. Ishii, Y. Kashima, Y. Kawakami, R. Kirste, M. Kneissl, R. Martin, F. Mehnke, M. Meneghini, A. Ougazzaden, P. J. Parbrook, S. Rajan, P. Reddy, F. Römer, J. Ruschel, B. Sarkar, F. Scholz, L. J. Schowalter, P. Shields, Z. Sitar, L. Sulmoni, T. Wang, T. Wernicke, M. Weyers, B. Witzigmann, Y.-R. Wu, T. Wunderer, and Y. Zhang, "The 2020 UV emitter roadmap," J. Phys. D: Appl. Phys. **53**(50), 503001 (2020).
4. S. Cuesta, A. Harikumar, and E. Monroy, "Electron beam pumped light emitting devices," J. Phys. D: Appl. Phys. **55**(27), 273003 (2022).
5. T. Hayashi, Y. Kawase, N. Nagata, T. Senga, S. Iwayama, M. Iwaya, T. Takeuchi, S. Kamiyama, I. Akasaki, and T. Matsumoto, "Demonstration of electron beam laser excitation in the UV range using a GaN/AlGaN multiquantum well active layer," Sci. Rep. **7**(1), 2944 (2017).
6. T. Wunderer, J. Jeschke, Z. Yang, M. Teepe, M. Batres, B. Vancil, and N. Johnson, "Resonator-length dependence of electron-beam-pumped UV-A GaN-based lasers," IEEE Photonics Technol. Lett. **29**(16), 1344–1347 (2017).
7. K. L. Shaklee and R. F. Leheny, "Direct determination of optical gain in semiconductor crystals," Appl. Phys. Lett. **18**(11), 475–477 (1971).
8. S. Cuesta, Y. Cure, F. Donatini, L. Denaix, E. Bellet-Amalric, C. Bougerol, V. Grenier, Q. M. Thai, G. Nogues, S. T. Purcell, L. S. Dang, and E. Monroy, "AlGaN/GaN asymmetric graded-index separate confinement heterostructures designed for electron-beam pumped UV lasers," Opt. Express **29**(9), 13084–13093 (2021).
9. S. M. Islam, K. Lee, J. Verma, V. Protasenko, S. Rouvimov, S. Bharadwaj, H. Xing, and D. Jena, "MBE-grown 232–270 nm deep-UV LEDs using monolayer thin binary GaN/AlN quantum heterostructures," Appl. Phys. Lett. **110**(4), 041108 (2017).
10. S. M. Islam, V. Protasenko, K. Lee, S. Rouvimov, J. Verma, H. Xing, and D. Jena, "Deep-UV emission at 219 nm from ultrathin MBE GaN/AlN quantum heterostructures," Appl. Phys. Lett. **111**(9), 091104 (2017).
11. Y. Liao, C. Thomidis, A. Bhattacharyya, C. Kao, A. Moldawer, W. Zhang, and T. D. Moustakas, "Development of Milliwatt Power AlGaN-based Deep UV-LEDs by Plasma-assisted Molecular Beam Epitaxy," MRS Proc. **1202**, 169–175 (2009).
12. M. Henini, ed., *Molecular Beam Epitaxy: From Research to Mass Production*, Second edition (Elsevier, 2018).
13. S. M. N. Hasan, W. You, M. S. I. Sumon, and S. Arafin, "Recent Progress of Electrically Pumped AlGaN Diode Lasers in the UV-B and -C Bands," Photonics **8**(7), 267 (2021).
14. Q. Zhang, X. Yin, and S. Zhao, "Recent Progress on Aluminum Gallium Nitride Deep Ultraviolet Lasers by Molecular Beam Epitaxy," Phys. Status Solidi RRL **15**(7), 2100090 (2021).
15. Y. Kotsar, B. Doisneau, E. Bellet-Amalric, A. Das, E. Sarigiannidou, and E. Monroy, "Strain relaxation in GaN/AlxGa1-xN superlattices grown by plasma-assisted molecular-beam epitaxy," J. Appl. Phys. **110**(3), 033501 (2011).
16. J. F. Muth, J. H. Lee, I. K. Shmagin, R. M. Kolbas, H. C. Casey Jr, B. P. Keller, U. K. Mishra, and S. P. DenBaars, "Absorption coefficient, energy gap, exciton binding energy, and recombination lifetime of GaN obtained from transmission measurements," Appl. Phys. Lett. **71**(18), 2572–2574 (1997).
17. J. Pastrňák and L. Roskovcová, "Refraction Index Measurements on AlN Single Crystals," phys. stat. sol. (b) **14**(1), K5–K8 (1966).
18. T. Kawashima, H. Yoshikaza, and S. Adachi, "Optical properties of hexagonal GaN," J. Appl. Phys. **82**(7), 3528–3535 (1997).
19. M. G. R. Martens, "Optical gain and modal loss in AlGaN based deep UV lasers," TU Berlin (2018).

Optics EXPRESS


20. W. Guo, Z. Bryan, J. Xie, R. Kirste, S. Mita, I. Bryan, L. Hussey, M. Bobea, B. Haidet, M. Gerhold, R. Collazo, and Z. Sitar, "Stimulated emission and optical gain in AlGaN heterostructures grown on bulk AlN substrates," J. Appl. Phys. **115**(10), 103108 (2014).
21. Q. Guo, R. Kirste, S. Mita, J. Tweedie, P. Reddy, B. Moody, Y. Guan, S. Washiyama, A. Klump, Z. Sitar, and R. Collazo, "Design of AlGaN-based quantum structuresfor low threshold UVC lasers," J. Appl. Phys. **126**(22), 223101 (2019).
22. S. Heppel, A. Hangleiter, S. Bader, G. Brüderl, A. Weimar, V. Kümmler, A. Lell, V. Härle, J. Off, B. Kuhn, and F. Scholz, "Systematics of Optical Gain in GaInN/GaN Laser Structures," phys. stat. sol. (a) **188**(1), 59–63 (2001).
23. T. Oto, R. G. Banal, M. Funato, and Y. Kawakami, "Optical gain characteristics in Al-rich AlGaN/AlN quantum wells," Appl. Phys. Lett. **104**(18), 181102 (2014).
24. M. Martens, *Optical gain and modal loss in AlGaN based deep UV lasers*, Technische Universität Berlin (2018).
25. E. Francesco Pecora, W. Zhang, A. Yu. Nikiforov, L. Zhou, D. J. Smith, J. Yin, R. Paiella, L. Dal Negro, and T. D. Moustakas, "Sub-250 nm room-temperature optical gain from AlGaN/AlN multiple quantum wells with strong band-structure potential fluctuations," Appl. Phys. Lett. **100**(6), 061111 (2012).
26. L. Dal Negro, P. Bettotti, M. Cazzanelli, D. Pacifici, and L. Pavesi, "Applicability conditions and experimental analysis of the variable stripe length method for gain measurements," Opt. Commun. **229**(1-6), 337–348 (2004).
27. S. Cuesta Arcos, Q. M. Thai, Y. Curé, F. Donatini, E. Bellet-Amalric, C. Bougerol, G. Nogues, S. T. Purcell, L. S. Dang, and E. Monroy, "Development of AlGaN/GaN heterostructures for e-beam pumped UV lasers," in *Gallium Nitride Materials and Devices XVI*, H. Morkoç, H. Fujioka, and U. T. Schwarz, eds. (SPIE, 2021), p. 15.
28. R. Kirste, Q. Guo, J. H. Dycus, A. Franke, S. Mita, B. Sarkar, P. Reddy, J. M. LeBeau, R. Collazo, and Z. Sitar, "6 kW/cm2 UVC laser threshold in optically pumped lasers achieved by controlling point defect formation," Appl. Phys. Express **11**(8), 082101 (2018).
29. M. Shan, Y. Zhang, T. B. Tran, J. Jiang, H. Long, Z. Zheng, A. Wang, W. Guo, J. Ye, C. Chen, J. Dai, and X. Li, "Deep UV Laser at 249 nm Based on GaN Quantum Wells," ACS Photonics **6**(10), 2387–2391 (2019).
30. X.-H. Li, T. Detchprohm, T.-T. Kao, Md. M. Satter, S.-C. Shen, P. Douglas Yoder, R. D. Dupuis, S. Wang, Y. O. Wei, H. Xie, A. M. Fischer, F. A. Ponce, T. Wernicke, C. Reich, M. Martens, and M. Kneissl, "Low-threshold stimulated emission at 249 nm and 256 nm from AlGaN-based multiple-quantum-well lasers grown on sapphire substrates," Appl. Phys. Lett. **105**(14), 141106 (2014).
31. H. Yoshida, M. Kuwabara, Y. Yamashita, Y. Takagi, K. Uchiyama, and H. Kan, "AlGaN-based laser diodes for the short-wavelength ultraviolet region," New J. Phys. **11**(12), 125013 (2009).
32. H. Yoshida, Y. Yamashita, M. Kuwabara, and H. Kan, "A 342-nm ultraviolet AlGaN multiple-quantum-well laser diode," Nat. Photonics **2**(9), 551–554 (2008).
33. J. Edmond, A. Abare, M. Bergman, J. Bharathan, K. Lee Bunker, D. Emerson, K. Haberern, J. Ibbetson, M. Leung, P. Russel, and D. Slater, "High efficiency GaN-based LEDs and lasers on SiC," J. Cryst. Growth **272**(1-4), 242–250 (2004).
34. S. Nagahama, T. Yanamoto, M. Sano, and T. Mukai, "Ultraviolet GaN Single Quantum Well Laser Diodes," Jpn. J. Appl. Phys. **40**(Part 2, No. 8A), L785–L787 (2001).
35. T. Sakai, M. Kushimoto, Z. Zhang, N. Sugiyama, L. J. Schowalter, Y. Honda, C. Sasaoka, and H. Amano, "On-wafer fabrication of etched-mirror UV-Claser diodes with the ALD-deposited DBR," Appl. Phys. Lett. **116**(12), 122101 (2020).
36. Z. Zhang, M. Kushimoto, T. Sakai, N. Sugiyama, L. J. Schowalter, C. Sasaoka, and H. Amano, "A 271.8 nm deep-ultraviolet laser diode for room temperature operation," Appl. Phys. Express **12**(12), 124003 (2019).
37. H. Yoshida, Y. Takagi, M. Kuwabara, H. Amano, and H. Kan, "Entirely Crack-Free Ultraviolet GaN/AlGaN Laser Diodes Grown on 2-in. Sapphire Substrate," Jpn. J. Appl. Phys. **46**(9A), 5782–5784 (2007).
38. S. Tanaka, Y. Ogino, K. Yamada, T. Omori, R. Ogura, S. Teramura, M. Shimokawa, S. Ishizuka, A. Yabutani, S. Iwayama, K. Sato, H. Miyake, M. Iwaya, T. Takeuchi, S. Kamiyama, and I. Akasaki, "AlGaN-based UV-B laser diode with a high optical confinement factor," Appl. Phys. Lett. **118**(16), 163504 (2021).
39. Y. Aoki, M. Kuwabara, Y. Yamashita, Y. Takagi, A. Sugiyama, and H. Yoshida, "A 350-nm-band GaN/AlGaN multiple-quantum-well laser diode on bulk GaN," Appl. Phys. Lett. **107**(15), 151103 (2015).
40. K. Sato, S. Yasue, K. Yamada, S. Tanaka, T. Omori, S. Ishizuka, S. Teramura, Y. Ogino, S. Iwayama, H. Miyake, M. Iwaya, T. Takeuchi, S. Kamiyama, and I. Akasaki, "Room-temperature operation of AlGaN ultraviolet-B laser diode at 298 nm on lattice-relaxed Al0.6Ga0.4N/AlN/sapphire," Appl. Phys. Express **13**(3), 031004 (2020).
41. K. Iida, T. Kawashima, A. Miyazaki, H. Kasugai, S. Mishima, A. Honshio, Y. Miyake, M. Iwaya, S. Kamiyama, H. Amano, and I. Akasaki, "350.9 nm UV Laser Diode Grown on Low-Dislocation-Density AlGaN," Jpn. J. Appl. Phys. **43**(No. 4A), L499–L500 (2004).
42. T. Wunderer, C. L. Chua, J. E. Northrup, Z. Yang, N. M. Johnson, M. Kneissl, G. A. Garrett, H. Shen, M. Wraback, B. Moody, H. S. Craft, R. Schlesser, R. F. Dalmau, and Z. Sitar, "Optically pumped UV lasers grown on bulk AlN substrates," Phys. Status Solidi C **9**(3-4), 822–825 (2012).
43. C. A. Klein, "Bandgap Dependence and Related Features of Radiation Ionization Energies in Semiconductors," J. Appl. Phys. **39**(4), 2029–2038 (1968).


134.214.240.35 {ts '2023-05-05 10:12:50'}